

Strain engineering of valley-polarized hybrid excitons in a 2D semiconductor

Abhijeet M. Kumar¹, Douglas J. Bock¹, Denis Yagodkin¹, Edith Wietek², Bianca Höfer¹, Max Sinner³, Pablo Hernández López⁴, Sebastian Heeg⁴, Cornelius Gahl¹, Florian Libisch³, Alexey Chernikov², Ermin Malic⁵, Roberto Rosati⁵, and Kirill I. Bolotin^{1*}

¹*Department of Physics, Freie Universität Berlin, Arnimallee 14, 14195 Berlin, Germany*

²*Institute of Applied Physics and Würzburg-Dresden Cluster of Excellence ct.qmat, Technische Universität Dresden, 01062 Dresden, Germany*

³*Institute for Theoretical Physics, TU Wien, Wiedner Hauptstraße 8-10, 1040 Vienna, Austria*

⁴*Department of Physics, Humboldt-Universität Berlin, Newtonstraße 15, 12489 Berlin, Germany and*

⁵*Department of Physics, Philipps-Universität Marburg, 35037 Marburg, Germany*

Abstract: Encoding and manipulating digital information in quantum degrees of freedom is one of the major challenges of today’s science and technology. The valley indices of excitons in transition metal dichalcogenides (TMDs) are well-suited to address this challenge. Here, we demonstrate a new class of strain-tunable, valley-polarized hybrid excitons in monolayer TMDs, comprising a pair of energy-resonant intra- and intervalley excitons. These states combine the advantages of bright intravalley excitons, where the valley index directly couples to light polarization, and dark intervalley excitons, characterized by low depolarization rates. We demonstrate that the hybridized state of dark KK’ intervalley and defect-localized excitons exhibits a degree of circular polarization of emitted photons that is three times higher than that of the constituent species. Moreover, a bright KK intravalley and a dark KQ exciton form a coherently coupled hybrid state under energetic resonance, with their valley depolarization dynamics slowed down a hundredfold. Overall, these valley-polarized hybrid excitons with strain-tunable valley character emerge as prime candidates for valleytronic applications in future quantum and information technology.

Introduction

The emerging field of valleytronics aims to use the valley index of quasiparticles to store and process quantum information. Transition metal dichalcogenides (TMDs) from the family of layered 2D semiconductors are promising valleytronic materials due to the presence of energy-degenerate extremal points in their band structure (e.g., at K and K’ or Q and Q’) that host electronic wavefunctions. The K and K’ valleys can be selectively addressed by light chirality via valley-contrasting optical selection rules [1, 2], with the bright energy-degenerate excitons, X_{KK} and $X_{K’K’}$ (subscripts denote valley indices of hole and electron wavefunctions, respectively) inheriting the valley index [3–6]. The polarization state of the emitted light provides a direct probe of the valley polarization of these excitons [5]. Experimental demonstrations of valley magnetization [7], coherent manipulation of valleys [8, 9], coupling between valley and spin [5, 10, 11], and spatial transport in TMDs [12–17] have firmly established the potential of these excitons for valleytronics.

Complex interactions among various intra- and intervalley excitons drive valley depolarization dynamics and transport in TMDs [12, 18–23]. The “bright” intravalley excitons X_{KK} and $X_{K’K’}$ suffer rapid valley depolarization due to radiative decay and intervalley exchange interactions on a timescale of picoseconds at cryogenic temperatures [24]. These excitons also interact with “dark” intervalley excitons, such as X_{KQ} or $X_{KK’}$, that form

the lowest excited state in tungsten-based TMDs [25–27]. The intervalley excitons weakly couple to light, and are protected from rapid exchange-induced depolarization [28, 29]. The spin/valley coupling at the Q valley [30], like at the K valley, adds further complexities to the dynamics associated with these states. Finally, momentum-delocalized energy bands slightly below the conduction band, caused by lattice defects, influence valley depolarization by providing the necessary momentum for the radiative recombination of intervalley excitons [31, 32]. Despite highly suitable properties of the intervalley excitons for valleytronics, controlling inter-excitonic interactions for the tunable valley polarization and dynamics in TMDs has remained largely unexplored.

Here, we employ mechanical strain as a powerful tool to modulate intervalley interactions and tune valley polarization dynamics in WSe_2 . Our idea builds on the emerging concept of valley-hybridized excitons, a new class of quasiparticles in TMD monolayers, that we recently demonstrated [32, 34]. The underlying principle involves strain-contrasting energy shift of different TMD valleys [33], that brings bright and dark excitons with distinct valley character into energetic resonance at specific strain values [35]. Crucially, valley-hybridized excitons present new means of controlling valley dynamics in TMDs, surpassing conventionally probed bright and dark excitons. First, valley-hybridized excitons can inherit the optical properties of the states constituting them, such as large oscillator strength and reduced intervalley exchange rate. Second, hybridization enhances light-matter interactions for the dark excitons, leading to a substantial increase in their optical detectability. This effectively overcomes the usual limitations of conventional techniques — that

* kirill.bolotin@fu-berlin.de

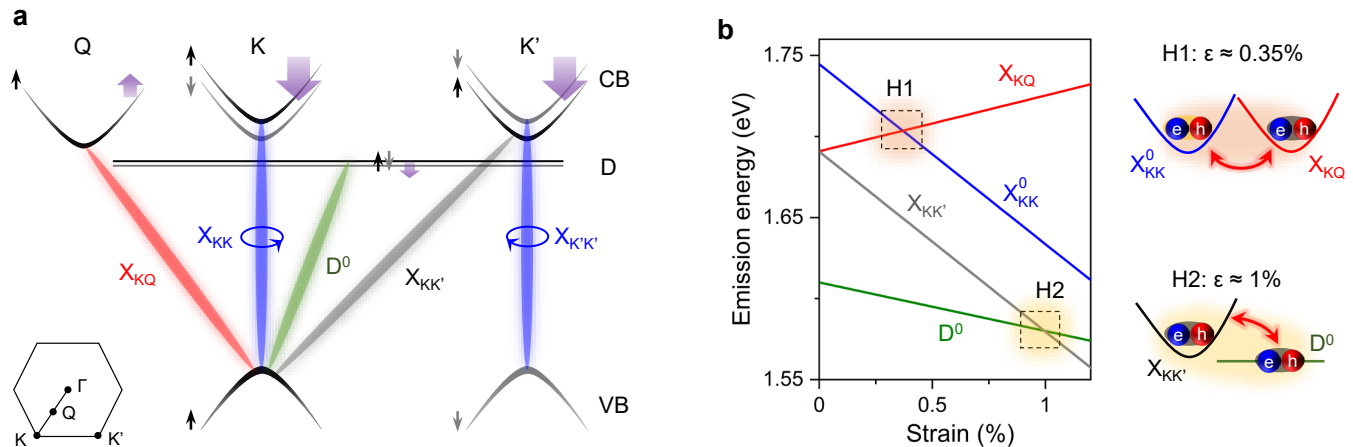


FIG. 1. **Exciton hybridization in 1L-WSe₂.** **a** Schematic band structure in 1L-WSe₂ at zero strain with selected excitonic transitions: X_{KK} and $X_{K'K'}$ (blue), X_{KQ} (red), $X_{KK'}$ (gray), D^0 (green). X_{KK} and $X_{K'K'}$ transitions couple to light with opposite chirality. The Q/Q' valleys are also spin/valley locked, similar to the K/K' valleys. The higher energy Q sub-band is not shown here due to a large spin-splitting (> 100 meV) [33]. Purple arrows denote strain response of valleys with respect to the valence band at the K valley. **b** Left panel: theoretically calculated strain response of excitons in 1L-WSe₂, same color-coding as in **a**. Excitons from different valleys enter energetic resonance near specific strain values, denoted by shaded regions H1 and H2. Note, these calculations do not account for the influence of hybridization on energy shift. Right panel: hybridized state of X_{KK}^0 and X_{KQ} at $\epsilon \approx 0.35\%$ (H1, top), $X_{KK'}$ and D^0 at $\epsilon \approx 1\%$ (H2, bottom) in excitonic representation.

are integrated with magnetic fields [36], surface plasmon polaritons [37], or waveguides [38] — in enhancing these interactions in devices without strain control. Finally, the valley-hybridized excitons are externally tunable by controlling the strain state of the device.

Leveraging this concept, we focus on the excitons associated with Q valley and momentum-delocalized defect states, which are controllably brought into energetic resonance with K/K' valley excitons in a monolayer of WSe₂. We find that the emitted photons from these valley-hybridized excitons retain circular polarization, indicating an associated valley index that can be read out via the optical selection rules for K/K' valleys. We examine the states arising from the hybridization between dark intervalley $X_{KK'}$ and defect-related excitons D^0 , near 0.8% strain. We observe a more than threefold increase in valley polarization of the resulting state, combined with an increase in the radiative recombination rate, compared to the dark excitons in a pristine device. We interpret this as a consequence of the lifting of momentum selection rules upon hybridization. Finally, we investigate the hybridized states of bright X_{KK}^0 and dark X_{KQ} excitons, at $\sim 0.3\%$ strain. We observe a substantial increase in the valley polarization and a remarkable hundredfold slowdown in the depolarization dynamics, which we assign to the suppressed exchange interactions in the resulting coherent state.

Results

Strain-controlled exciton hybridization. A schematic band structure of an unstrained 1L-WSe₂ and selected excitonic transitions are shown in Figure 1a. The optically bright neutral excitons X_{KK}^0 and

$X_{K'K'}^0$ (blue in Fig. 1a) reside energetically above the intervalley excitons $X_{KK'}$ (gray) and X_{KQ} (red). A defect-localized exciton D^0 (green) is associated with momentum-delocalized energy bands, arising due to point defects, such as single selenium vacancies. The $X_{KK'}$ and X_{KQ} excitons are characterized by weak oscillator strengths, and require a third particle (e.g., impurity, phonons, etc.) for radiative recombination [26, 39–42]. As the defects break translational symmetry, radiative recombination of D^0 is allowed; however, its emission intensity is influenced by the defect density.

An applied mechanical strain, ϵ , changes the energetic alignment of valleys, which modifies optical response of all excitonic species [43–46]. Under tensile biaxial strain, different valleys exhibit contrasting energy shifts determined by the distinct orbital composition of each valley [33, 47]. Specifically, the conduction band (CB) at the K/K' and Q valleys exhibits opposite energy shift with respect to the energies of the valence band (VB) at the K/K' valleys [34, 35], while the defect energy bands (D) remain weakly affected (purple arrows in Fig. 1a) [31]. Critically, various intra- and intervalley excitons inherit the strain response of the valleys that host their respective electron and hole wavefunctions. Figure 1b shows theoretically calculated strain response of selected excitons in a 1L-WSe₂. Near 0.35% strain, the dark exciton X_{KQ} enters energetic resonance with the bright exciton X_{KK}^0 (region H1 in Fig. 1b) and acquires oscillator strength [34]. Consequently, the resulting hybridized state is optically bright, and shows a distinct optical signature, with its emission energy independent of strain (see Note S1 for details) [34]. Near 1% strain, the inter-

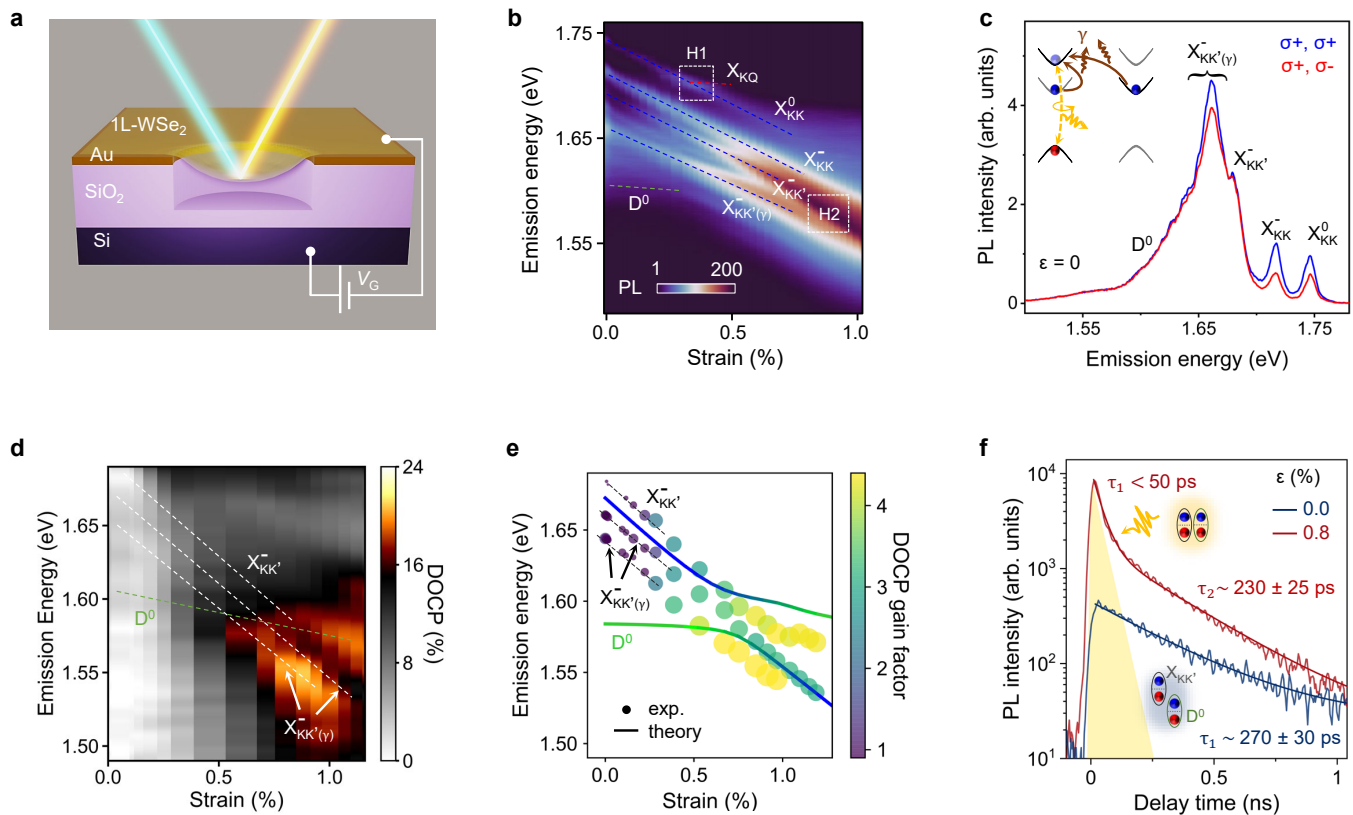


FIG. 2. Strain tuning of dark K/K' valley exciton polarization. **a** Schematic of the electrostatic straining technique. An applied gate voltage V_G induces biaxial strain in the center of the membrane. **b** PL vs. strain false color map in 1L-WSe₂ (device 1) at $T = 10$ K. The energy shifts of excitons and the hybridization regimes are labeled. **c** Co- and cross-polarized PL spectra (blue and red, respectively) from 1L-WSe₂ at $\epsilon = 0$ under $\sigma+$ excitation (see Note S4 for discussions on the influence of doping-related effects on *DOCP*). The inset shows radiative emission channels for dark trions $X_{KK'}^-$, mediated by chiral phonons (brown arrows). **d** *DOCP* vs. strain false color map in 1L-WSe₂ (acquired in a different V_G sweep than in **b**) for the states below 1.70 eV. White dashed lines denote the energy shift of $X_{KK'}^-$, and its two phonon replicas; green line extrapolates the same for D^0 . **e** Scatter plot for the emission energy vs. strain for $X_{KK'}^-$, and its phonon replicas; the area of the circle is proportional to the *DOCP*, the *DOCP* gain factor (η) for each state is color-coded. Theoretically calculated strain response of $X_{KK'}^-$, and D^0 (solid lines), accounting for hybridization effects, reveal an avoided-crossing pattern; color of the line corresponds to the valley character of each exciton (blue: $X_{KK'}^-$, green: D^0), both lines are downshifted by 15 meV for clarity. **f** Time-resolved PL traces in the energetic vicinity of $X_{KK'}^-$, at zero strain (blue) and 0.8% strain (red) from the same device. PL intensity at $t = 0$ increases and a new decay component emerges at 0.8% strain, highlighted by yellow-shaded region; cartoons depict relative energetic alignment of $X_{KK'}$ and D^0 excitons.

valley excitons $X_{KK'}$ hybridize with D^0 (H2 in Fig. 1b). In this scenario, defect states are predicted to lift momentum selection rules, enabling radiative recombination of the otherwise dark $X_{KK'}$ excitons [31, 32]. Their hybridization is further characterized by an avoided crossing of the excitonic energy levels and a broken spin/valley locking near the K and K' valleys in the CB [31]. Overall, the hybridized species acquire traits from the constituting excitons with different valley characters, with the intervalley interactions being strain-dependent. Therefore, we expect exciton hybridization to strongly influence the spin/valley dynamics of excitons in 1L-WSe₂, with strain playing a key role in controlling these effects.

Optical detection of valley-hybridized excitons.

To induce the mechanical strain required to form valley-hybridized excitons, we employ an electrostatic gating-

based straining technique that we recently developed [32, 34]. A monolayer of WSe₂ is suspended over a circular trench of diameter $\sim 5 \mu\text{m}$ in an Au/SiO₂/Si substrate (Fig. 2a). A gate voltage (V_G) applied between WSe₂ and Si deflects the membrane, inducing tensile biaxial strain in its center, which is symmetric for both polarity of V_G . It is important to note that, although carrier density is inherently linked to the strain state in our approach (see Note S4 for details), the effects of strain on excitonic energies can be readily distinguished from those originating from carrier density changes [32, 34]. We record the excitons' photoluminescence (PL) response vs. strain at $T = 10$ K under a CW laser excitation at 1.84 eV (Fig. 2b; see *Methods* for details). In addition to the well-known bright excitonic states, we identify a series of dark intervalley excitons at

$\epsilon = 0$, including intervalley trions ($X_{\text{KK}'}^-$) near 1.685 eV, their phonon replicas ($X_{\text{KK}'(\gamma)}^-$) around 1.65–1.67 eV and defect-related excitons near 1.60 eV by comparing their energetic positions and power dependence with previous reports [32, 34, 48, 49].

Upon applying strain, we observe substantial changes in the PL intensity and emission energy of excitons (Fig. 2b). By tracking the emission energy vs. applied strain and comparing them with the theoretical predictions for the evolution of excitonic energies with strain (Fig. 1b), we identify two hybridization regimes H1 and H2. First, near 0.35% strain, the dark X_{KKQ} becomes energy-resonant with the bright X_{KK}^0 exciton and partially brightens due to hybridization (Fig. S8) [34]. Second, near 0.8% strain, the intervalley $X_{\text{KK}'}$ excitons hybridize with D^0 , gaining oscillator strength (Fig. S4) [31, 32]. Consequently, their PL intensity increases by more than an order of magnitude compared to the unstrained state (Fig. 2b). The properties of these hybridized states are detailed in our recent reports [32, 34].

To probe the valley polarization of excitons under strain, we employ polarization-resolved PL measurements under circular or linear excitation. The retention of an exciton's valley memory over its lifetime is quantified by the degree of circular polarization, $DOCP = \frac{I_{\text{co}} - I_{\text{cross}}}{I_{\text{co}} + I_{\text{cross}}}$, where I_{co} and I_{cross} are the co- and cross-polarized PL intensities under circularly polarized excitation, respectively. We note that, unlike the case of bright neutral (X_{KK}^0) and charged ($X_{\text{KK}}^{+/-}$) excitons, the valley-selective optical selection rules do not directly apply to the intervalley and defect-related transitions. Nevertheless, previous works have demonstrated that the experimentally measured $DOCP$ reliably characterizes their valley polarization state [38, 50], forming the basis to probe the valley polarization of individual states in our device.

Conversely, the degree of linear polarization, $DOLP = \frac{I_{\text{H}} - I_{\text{V}}}{I_{\text{H}} + I_{\text{V}}}$, where I_{H} and I_{V} are the two orthogonal linearly polarized PL components, provides information about the quantum coherence of the entangled states across the two valleys [8]. The $DOLP$ is non-zero only for X_{KK}^0 (Fig. S8). Valley coherence for dark- and many-body excitons is suppressed due to processes such as intervalley scattering [8] and long lifetimes compared to X_{KK}^0 [51], resulting in the vanishing of their $DOLP$.

Polarization control of hybridized $X_{\text{KK}'}$ - D^0 excitons. Having demonstrated the concept of strain-controlled exciton hybridization, we now investigate the valley-polarized response of K/K' intervalley excitons as they enter energetic resonance with D^0 (region H2 in Figs. 1b, 2b). Figure 2c shows co- and cross-circularly polarized PL in 1L-WSe₂ at zero strain. In this case, $X_{\text{KK}'}$ excitons show vanishing $DOCP$, consistent with their out-of-plane transition dipoles [49, 52, 53]. A small $DOCP < 5\%$ observed from $X_{\text{KK}'(\gamma)}^-$ is likely associated with intervalley scattering processes involving chiral phonons (inset of Fig. 2c) [49], impurities [48], or resident carriers [54]. No $DOCP$ is observed from defect-related

states near 1.60 eV. When strain is applied, the $DOCP$ for these states changes drastically (Fig. 2d). To quantify these changes, we plot the emission energy vs. strain for selected dark states $X_{\text{KK}'}$ and $X_{\text{KK}'(\gamma)}^-$, obtained using the fitting procedure described in Ref. [34], in Fig. 2e; the color of the data points reflects the $DOCP$ gain factor η , defined as $\eta = \frac{DOCP(\epsilon)}{DOCP(\epsilon=0)}$. Note that an experimental uncertainty in $DOCP$ of 5% is assumed to calculate η for states with vanishing $DOCP$ at zero strain.

We make the following observations from the data in Fig. 2e. First, a maximum in $DOCP$ (η between 3 and 5) for dark trions and their phonon replicas is reached at state-specific strain values between 0.7 and 1%, coinciding with the point of hybridization of these states with D^0 . This behaviour also mimics the PL intensity response of the same states, which reaches its maximum in the same strain regime (Fig. 2b). Second, the slope of strain-dependent energy shift for the highest energy dark trions changes for $\epsilon > 1\%$, aligning with the trend of D^0 excitons. This suggests that the dark trions acquire, at least partially, the character of D^0 , yet, surprisingly, retain their valley polarization. This change in the valley character is confirmed by our first principle calculations that show an avoided crossing behaviour between the two states (solid lines in Fig. 2e) by accounting for strain-dependent coupling between them (see Note S2, Fig. S3 for details).

Finally, we find that the temporal dynamics of the dark trions, recorded via time-resolved PL (see *Methods* for details), change significantly near the hybridization point (Fig. 2f). At $\epsilon = 0.8\%$, the PL intensity at $t = 0$ increases tenfold, accompanied by the emergence of new decay component ($\tau_1 < 50$ ps), indicating a similar increase in the recombination rate compared to the zero strain case. This directly reflects the increase of the light-matter coupling strengths due to exciton hybridization and demonstrates the associated increase in the radiative recombination rate.

The data in Figs. 2d-f collectively highlight the influence of inter-excitonic hybridization on the valley polarization of dark K/K' valley excitons. The amplification in $DOCP$ is concomitant with a maximum in PL intensity, reduced radiative lifetime, and an avoided crossing between the defect-bound and the dark K/K' valley excitons. This is consistent with resonant coupling with defects relaxing the momentum-selection rules, driving radiative recombination of dark excitons and enabling direct optical detection of their valley polarization. The faster recombination prevents the mixing of valley states in the hybridized species, leading to an enhanced $DOCP$. The valley polarization is further strengthened by the hole's valley state in the VB, which predominantly resides in the valley of excitation. Notably, the D^0 exciton retains valley polarization up to the maximum applied strain level of 1.8% (Fig. S4), indicating that this state has inherited the valley character of 'free' K/K' valley excitons after hybridization. Finally, we note that while the straining technique also changes the carrier density

in these devices, such effects do not explain the observed amplification in *DOCP* (see Note S4 and Figs. S5, S6 for details).

Polarization control of hybridized X_{KK}^0 - X_{KQ} excitons. Next, we focus on the hybridized state of X_{KQ} and X_{KK}^0 excitons (region H1 in Figs. 1b, 2b), which is characterized by a new peak in the PL spectrum near 1.70 eV and near 0.35% strain (Fig. S8) [34]. Both the strain range and the spectral window of this hybridization are different than the previously discussed regime H2, corresponding to the $X_{\text{KK}'}-D^0$ hybridization.

Figures 3a and 3b show false color maps of *DOCP* and *DOLP* vs. strain, respectively, in the energetic vicinity of X_{KK}^0 . We detect an increase in both *DOCP* and *DOLP* in the regime corresponding to the formation of the hybridized state. Since the retention of linear polarization is a measure of exciton valley coherence, the observation of an increased *DOLP* suggests that the energy-resonant X_{KK}^0 and X_{KQ} have formed a coherently-coupled hybrid state. An increased *DOCP* also suggests the coupling between the valley indices of the excitons from K and Q valleys, which has remained unexplored until now.

To explain our observations, we develop a many-particle theory to microscopically determine the strain-dependent exciton landscape, both with and without exciton hybridization. Starting from exciton dynamics in the presence of exchange interactions [29] and doping [55], we include the continuous-wave excitation to obtain the relative occupation of the bright excitons with opposite circular polarization (see *Methods* and Note S1). This allows us to write the *DOCP* as

$$DOCP = \frac{\Gamma_{\text{dec}}}{2\Gamma_{\text{exc}} + \Gamma_{\text{dec}}}, \quad (1)$$

where $\Gamma_{\text{dec}} = \Gamma_{\text{rad}} + \Gamma_{\text{sc}}$ represents the combined rates associated with the radiative decay of excitons (Γ_{rad}) and phonon-assisted intervalley scattering (Γ_{sc}), while excluding the intervalley exchange rate Γ_{exc} . In the absence of hybridization, the latter decay rate is microscopically evaluated as $\Gamma_{\text{exc}} = \frac{2}{\Gamma_{\text{sc}}} J^2$, where $J^2 = \sum_{\mathbf{q}} |J_{\mathbf{q}}|^2 N_{\mathbf{q}}^0$ is the squared modulus of the exchange Hamiltonian $|J_{\mathbf{q}}|^2$, summed over the exciton momentum \mathbf{q} and weighted by the normalized excitonic distribution, here assumed to be thermalized (Note S1). In agreement with the generalized Maialle-Silva-Sham model [56, 57], the derived Γ_{exc} is quadratic in the exchange Hamiltonian — which depends weakly on strain — and scales with the inverse of the scattering rates Γ_{sc} . We further evaluate Γ_{sc} microscopically, revealing its crucial dependence on strain and hybridization. Our final calculations for the *DOCP* of X_{KK}^0 , via Eq. (1), show strong strain-dependent behaviour (Fig. 3c, top panel). Note, that the evaluation of *DOCP* via Eq. (1) is consistent with an independently employed rate equation model [5, 58].

In the absence of hybridization, our microscopic calculations show a decrease of *DOCP* with increased strain, with two pronounced drops near 0.15% and 0.27%

strain (dashed lines in Fig. 3c, top). These features reflect the strain-induced closing of optical and acoustic phonon-assisted scattering channels between X_{KK}^0 and X_{KQ} (Note S1). Consequently, the decay rate Γ_{dec} and, hence, the *DOCP* lowers. Notably, the *DOCP* increases sharply near $\epsilon = 0.35\%$ when the hybridization between X_{KK}^0 and X_{KQ} is accounted for in the model (red in Fig. 3c, top). Thanks to this hybridization, the bright states acquire a KQ component and, subsequently, gain the scattering channel from KQ to KK'. This scattering mechanism is particularly effective in this strain regime, as demonstrated recently by strain-dependent diffusion studies [59]. In contrast, the scattering between X_{KK}^0 and $X_{\text{KK}'}$ changes only weakly with strain due to their similar strain-dependent energy shifts (Fig. S2). We also assume negligible changes in the radiative decay rate Γ_{rad} of X_{KK}^0 as its binding energy remains nearly unaffected in the studied strain range [34]. Consequently, this new scattering channel between the hybridized states and $X_{\text{KK}'}$ leads to the increase of Γ_{dec} (depicted by the cartoon in Fig. 3d), and with it, to a local maximum in *DOCP* at $\sim 0.4\%$ strain.

Our experimental observations in Fig. 3c (bottom panel) are in qualitative agreement with the theoretical predictions. Furthermore, our theory also explains a gradual decrease of *DOCP* vs. strain for the hybridized state in experiments, which we ascribe to the residual inhomogeneity of the strain profile in our device (see Note S1, Fig. S1 for details).

Ultrafast dynamics of hybridized X_{KK}^0 - X_{KQ} excitons. Finally, our straining technique provides direct access to the investigation of spin/valley dynamics stemming from the resonant coupling between K and Q valley excitons. To this end, we employed single-color time-resolved Kerr rotation (TRKR) spectroscopy. Here, a circularly polarized pump pulse initializes a valley-polarized optical transition near the X_{KK}^0 resonance, while the spin/valley imbalance is probed by a time-delayed linearly polarized probe pulse (see *Methods* and Fig. S9 for details). We chose the temperature $T = 100$ K to minimize the contributions from dark excitons [22, 60], resident carriers [23, 61, 62], and trap states [23, 63], that are dominant at cryogenic temperatures and complicate the interpretation of the data.

Figure 4 shows TRKR traces at selected strain values; solid lines are the fits to the data. We observe a rapid decay of the TRKR signal at zero strain, with a time constant smaller than 2 ps (top panel). The TRKR dynamics change significantly near $\epsilon = 0.3\%$, the value corresponding to X_{KK}^0 - X_{KQ} resonance (middle panel). Here, the decay dynamics turn bi-exponential, with the second decay component (τ_2) longer-lived compared to the unstrained case by more than two orders of magnitude. As the applied strain is increased to 0.7%, the TRKR signal decay accelerates again, becoming qualitatively similar to the unstrained case, with a single decay constant of 2.4 ± 1 ps (bottom panel).

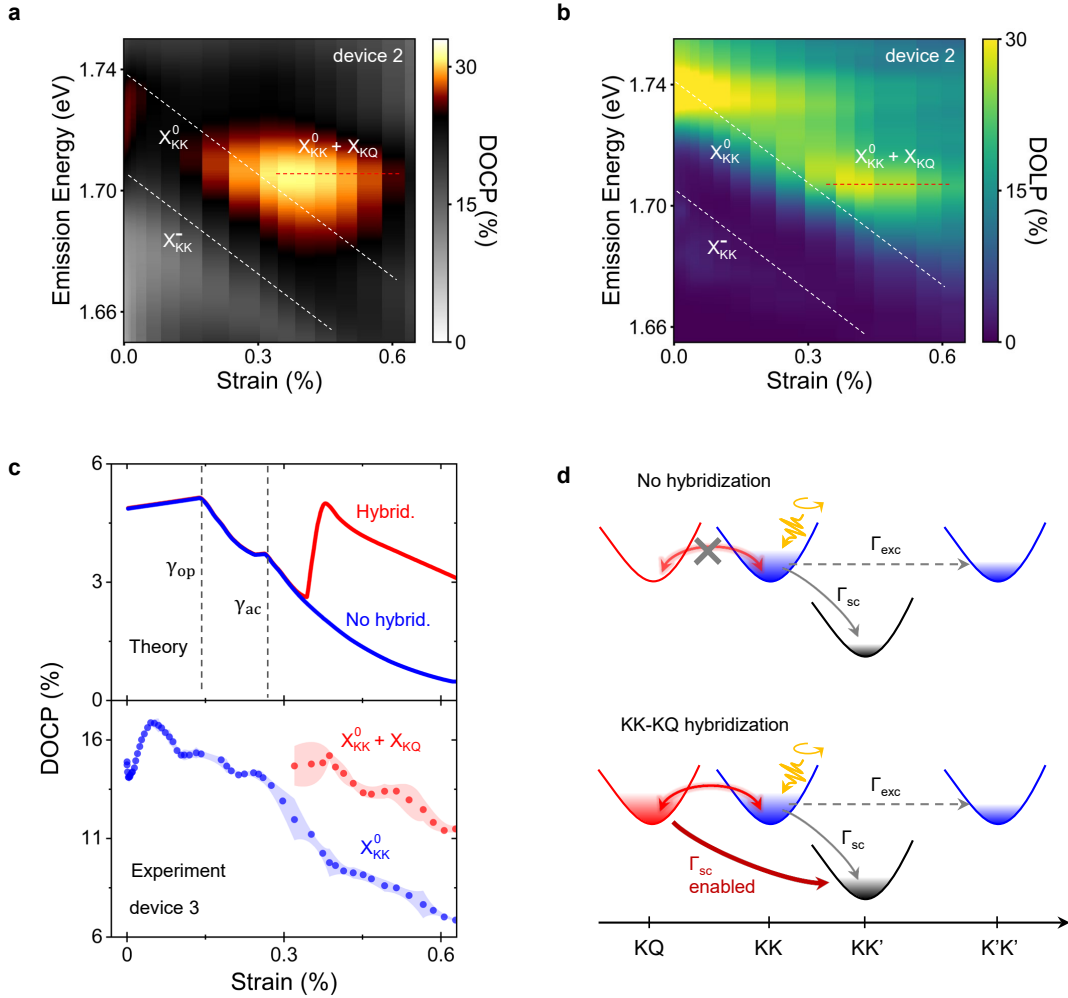


FIG. 3. **Valley polarization control by tuning KK–KQ coupling.** **a,b** False color map of *DOCP* (**a**) and *DOLP* (**b**) vs. strain from device 2. A local maximum in *DOCP* and *DOLP* is observed near 0.4% strain, suggesting an enhanced intervalley coupling and the formation of a coherent hybridized state. Note, the nonzero polarization on the higher energy tail arises from excitons located away from the membrane center due to strain inhomogeneity. **c** Top panel: theoretically calculated *DOCP* vs. strain for X_{KK}^0 without (blue) and with (red) hybridization with X_{KQ} . The two dashed lines denote strain values corresponding to the closing of optical (γ_{op})- and acoustic phonon (γ_{ac})-mediated scattering channel between X_{KK}^0 and X_{KQ} . Bottom panel: experimentally obtained *DOCP* vs. strain (from device 3). An increase in *DOCP* near 0.4% strain is observed for the hybridized state (red), showing qualitative agreement with the theory. The *DOCP* trend below 0.1% strain is not yet understood. **d** Schematic representation of intervalley exciton scattering near $\epsilon = 0.35\%$. X_{KK}^0 , $X_{K'K'}^0$, and X_{KQ} are energy-resonant, lying above $X_{KK'}$. Yellow arrows denote the valley polarized excitation of KK excitons, whereas gray arrows denote intervalley exchange (dashed) and phonon-assisted scattering (solid). In absence of hybridization (top), phonon-assisted scattering between X_{KK}^0 and X_{KQ} is blocked. The hybridization (bottom) forms a resonantly coupled KK–KQ state and enables a new scattering channel between X_{KQ} and $X_{KK'}$ (dark red arrow).

A short-lived TRKR dynamics at zero strain can be explained by rapid exchange-mediated intervalley scattering — expected to be dominant under resonant pump excitation — and phonon-mediated valley depolarization. We ascribe the long-lived TRKR dynamics near $\epsilon = 0.3\%$ to KK–KQ hybridization. Here, the KK state acquires a partially intervalley character, for which the exchange scattering mechanism is suppressed [29]. Correspondingly, the second decay component reflects a low rate of valley depolarization for the hybridized population. This

assignment is further supported by a similar trend consistently recorded across devices with varying doping levels, when probed near the X_{KK}^0 resonance and near 0.3% strain (Figs. S11, S12). The TRKR dynamics probed near the $X_{KK}^{+/-}$ resonance do not exhibit any long-lived component, with their decay constants ranging from 2 to 6 ps across the applied gate voltage range (Fig. S10). These findings rule out the the dynamics near $\epsilon = 0.3\%$ being governed by doping-related resident carrier depolarization [23, 61, 62]. Furthermore, the spin/valley dy-

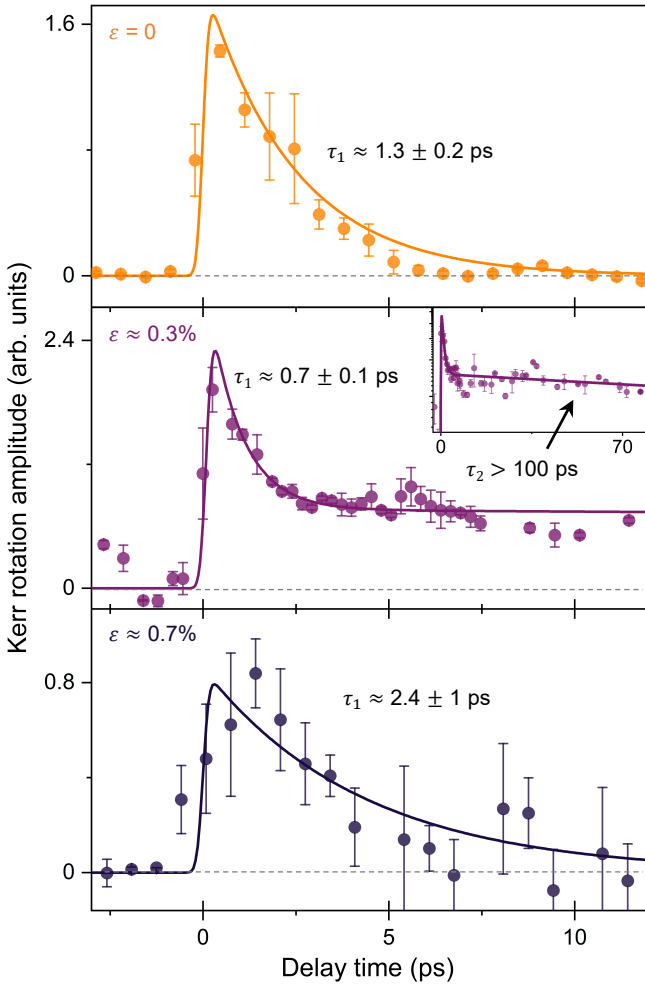


FIG. 4. **Ultrafast spin/valley dynamics vs. strain.** Top-bottom: TRKR dynamics in 1L-WSe₂ (device 2) at $\epsilon = 0, 0.3$ and 0.7% , respectively, at $T = 100$ K. The pump and probe energies ($E_{\text{pump}} = E_{\text{probe}}$) were set near the neutral exciton resonance for each strain value (1.730, 1.695, and 1.650 eV, respectively), determined via *in-situ* PL measurements. Solid lines are fits, dashed gray lines correspond to zero TRKR amplitude. The inset in the middle panel show the TRKR trace at $\epsilon = 0.3\%$ on a longer timescale in a semi-log plot. A second decay component with a time constant exceeding 100 ps is observed.

namics in our devices are free from substrate-related disorder, which are typically linked to doping-dependent transitions between mono- and bi-exponential decay profiles [63]. Finally, the disappearance of the long-lived component in the TRKR dynamics at 0.7% strain (bottom panel in Fig. 4) is consistent with X_{KK}^0 and X_{KQ} coming out of energetic resonance. Overall, our observations in Fig. 4 demonstrate the immense potential of strain in tuning ultrafast spin/valley dynamics in TMDs.

Discussion

To summarize, we demonstrated the emergence of valley-polarized hybrid excitons in WSe₂ monolayers under con-

trolled strain. By employing polarization-resolved spectroscopy, we recorded a more than threefold increase in the valley polarization of dark K/K' valley excitons upon hybridization with defect-related excitons. The hybridization with the KQ intervalley excitons increases the valley polarization of X_{KK}^0 excitons and reduces their spin/valley depolarization rates by more than two orders of magnitude.

Our findings include a first spectroscopic demonstration of strain-controlled intervalley coupling on valley polarization dynamics, and open multiple directions for future research. First, it may be possible to achieve near 100% valley polarization of hybridized excitons in future experiments with tunable, near-resonant excitation. We highlight that the reported valley polarization in our PL experiments is underestimated by up to 50% due to strain-induced energy detuning under fixed excitation energy (Fig. S7). Long lifetimes of species associated with the Q valley may be utilized for spin/valley-polarized transport, achievable in devices with engineered strain gradients. Second, our results opens new paths for theoretical exploration, particularly in understanding the microscopic interactions between excitons and phonons in the presence of defects, as well as the spin/valley depolarization mechanisms for the hybridized KK-KQ excitons. Finally, an exciting prospect is to describe the valley index in the language of pseudospin, where the effect of uniaxial strain is equivalent to that of a magnetic field acting in the pseudospin space [55, 64, 65]. We recently demonstrated this pseudomagnetic field exceeding 40 Tesla in uniaxially-strained TMDs, enabling the study of analogs of the Zeeman and Larmor effects, as well as tunable exciton coherence dynamics [66]. Investigating the coherent nature of KK-KQ excitons under pseudomagnetic fields [67] would be an interesting next step towards valley manipulation.

Methods

Sample fabrication The WSe₂ flakes were mechanically exfoliated and transferred onto a circular trench (diameter is $\sim 5 \mu\text{m}$) in a Au/Cr/SiO₂/Si stack using a dry transfer approach. The cavity was developed via wet etching process using Hydrofluoric (HF) acid. A gate voltage (typically in the range of up to ± 210 V) was applied between the TMD flake (electrically grounded) and the Si back gate of the chip to induce strain. The strain in the center was characterized following the laser interferometry approach used in our recent work [34].

Polarization-resolved PL measurements The devices were measured inside a cryostat (CryoVac Konti Micro) at a base temperature of 10 K. Devices 1 and 2 (corresponding to data in Figs. 2 and 3a,b) were probed under a CW laser excitation at $\lambda = 670$ nm ($6 \mu\text{W}$), tightly focused in the center of the membrane with spot diameter $\sim 1 \mu\text{m}$. For device 3 (data in Fig. 3c), we used a CW laser with $\lambda = 685$ nm and $2 \mu\text{W}$ power. A combination of a polarizer (GL 10, Thorlabs) and a quarter-wave plate

(RAC4.4.10, B. Halle) was used to control the circular polarization of excitation. For linearly-polarized excitation, the quarter-wave plate was replaced with a half-wave plate (RAC4.2.10, B. Halle). Both wave plates were positioned before the objective, ensuring that the emitted light passed through them before getting detected. To filter the polarization state of the emitted light, we used a combination of a half-wave plate and an analyzer before the spectrometer. The PL signal was detected using the Spectrometer Kymera 193i Spectrograph.

Time-resolved PL measurements The sample was excited by a pulsed Ti:sapphire laser (Coherent Chameleon Ultra II, 140 fs pulse duration and 80 MHz repetition rate) at $\lambda = 700$ nm and $0.55 \mu\text{Jcm}^{-2}$ fluence, with a laser spot of $\sim 1 \mu\text{m}$ diameter, focused onto the sample using a 60x objective. The injected electron-hole pair density was on the order of 10^{10}cm^{-2} , where Auger-like exciton-exciton annihilation effects are negligible. A streak camera (C10910, Hamamatsu) was used to time- and spectrally resolve the PL signal.

Time-resolved Kerr rotation microscopy We used a wavelength-tunable pulsed Ti:sapphire laser (Coherent Chameleon Ultra II, 140 fs pulse duration and 80 MHz repetition rate). The laser pulse was split into the pump and probe components. Circular polarization of the pump pulse was controlled using a combination of a linear polarizer and a quarter wave plate. Both the pulses were made collinear while being spatially separated, and were focused onto the sample at near normal incidence using a reflective objective (LMM40X-P01, Thorlabs). The pump and probe spot sizes were ~ 3 and $\sim 1 \mu\text{m}$, respectively. The reflected pump beam was blocked using a spatial filter. The reflected linearly-polarized probe was separated into two components of orthogonal polarization after passing through an optical bridge consisting of a half-wave plate and a Wollaston prism (Fig. S9). Both polarization components were simultaneously recorded by using a home-built balanced photodetector, and the differential signal was read out using a lock-in amplifier phase-locked to a chopper in the pump path. For all TRKR measurements, two traces with opposite pump helicity were recorded sequentially, and the average of these traces was calculated. The strain level and corresponding exciton resonances during the TRKR measurements were characterized by *in-situ* PL (Fig. S9).

Microscopic many-particle modeling We calculate exciton energies by solving a strain-dependent Wannier equation [34, 59], including the Keldysh-Rytova Coulomb potential [68, 69], and single-particle valley-dependent masses and strain-induced energy shifts [33, 35, 70]. The resulting excitonic eigenstates allow to evaluate the corresponding valley-dependent exciton-phonon scattering rates [59]. Assuming that hybridization occurs for quasi-resonant KK and KQ states, we are able to predict experimentally measured strain-dependent PL signatures. In order to predict the *DOCP*, we evaluate the relative occupation of bright exciton states with opposite circular polarization. For this purpose, we start from exciton dy-

namics in the presence of exchange interaction [29] and doping [55] and include the continuous-wave excitation. More details can be found in the Supplementary Information (Note S1).

Acknowledgments

The research group from Freie Universität Berlin acknowledges the Deutsche Forschungsgemeinschaft (DFG) for financial support through the Collaborative Research Center TRR 227 Ultrafast Spin Dynamics (project B08) and the Priority Programme SPP 2244 2DMP (project BO 5142/5) as well as the Federal Ministry of Education and Research (BMBF, Projekt 05K22KE3). The Marburg group acknowledges financial support by the DFG via SFB 1083 (project B9) and the regular project 512604469. The Dresden group acknowledges financial support by the DFG via SPP2244 (CH 1672/3, Project-ID: 443405595), joint project with the Marburg team (Project-ID: 287022282), SFB 1277 (Project B05, Project-ID No. 314695032), ERC CoG CouENGINE (GA number 101001764) and Würzburg-Dresden Cluster of Excellence on Complexity and Topology in Quantum Matter ct.qmat (EXC 2147, Project-ID 390858490). Research by the Vienna group has been supported by The Austrian Science Fund (FWF) through doctoral college TU-DX (DOC 142-N) and the MECS cluster of excellence 10.55776/COE5 MECS. For the purpose of open access, the author has applied a CC BY public copyright licence to any Author Accepted Manuscript version arising from this submission. The Humboldt-Universität Berlin group acknowledges funding from the DFG under the Emmy Noether Initiative (project-ID 433878606). We thank N. Stetzuhn and A. Dewambrechies for useful comments.

Author Contributions

A.M.K. and K.I.B. conceived the project. A.M.K., C.G., and D.Y. designed the experimental setup. A.M.K., D.J.B., B.H., and P.H.L. prepared the samples. S.H. and P.H.L. developed the electrostatic straining technique. A.M.K., D.J.B., and D.Y. performed polarization-resolved PL and TRKR measurements. E.W. and A.C. performed time-resolved PL measurements. R.R. and E.M. developed theory for KQ excitons. M.S. and F.L. developed the theory for defect excitons. A.M.K., D.B., E.W., and D.Y. analyzed the data. A.M.K., K.I.B., and R.R. wrote the manuscript with input from all co-authors.

Data Availability Statement

The data that support the findings of this study are available from the corresponding author upon reasonable request.

The authors declare no competing interest.

References

- [1] D. Xiao, G.-B. Liu, W. Feng, X. Xu, and W. Yao, *Physical Review Letters* **108**, 196802 (2012), publisher: American Physical Society.
- [2] T. Cao, G. Wang, W. Han, H. Ye, C. Zhu, J. Shi, Q. Niu,

- P. Tan, E. Wang, B. Liu, and J. Feng, *Nature Communications* **3**, 887 (2012), publisher: Nature Publishing Group.
- [3] K. He, N. Kumar, L. Zhao, Z. Wang, K. F. Mak, H. Zhao, and J. Shan, *Physical Review Letters* **113**, 026803 (2014), publisher: American Physical Society.
- [4] G. Wang, A. Chernikov, M. M. Glazov, T. F. Heinz, X. Marie, T. Amand, and B. Urbaszek, *Reviews of Modern Physics* **90**, 021001 (2018), publisher: American Physical Society.
- [5] K. F. Mak, K. He, J. Shan, and T. F. Heinz, *Nature Nanotechnology* **7**, 494 (2012), publisher: Nature Publishing Group.
- [6] K.-Q. Lin, J. D. Ziegler, M. A. Semina, J. V. Mamedov, K. Watanabe, T. Taniguchi, S. Bange, A. Chernikov, M. M. Glazov, and J. M. Lupton, *Nature Communications* **13**, 6980 (2022), publisher: Nature Publishing Group.
- [7] M. Onga, Y. Zhang, T. Ideue, and Y. Iwasa, *Nature Materials* **16**, 1193 (2017), publisher: Nature Publishing Group.
- [8] A. M. Jones, H. Yu, N. J. Ghimire, S. Wu, G. Aivazian, J. S. Ross, B. Zhao, J. Yan, D. G. Mandrus, D. Xiao, W. Yao, and X. Xu, *Nature Nanotechnology* **8**, 634 (2013), publisher: Nature Publishing Group.
- [9] K. Hao, G. Moody, F. Wu, C. K. Dass, L. Xu, C.-H. Chen, L. Sun, M.-Y. Li, L.-J. Li, A. H. MacDonald, and X. Li, *Nature Physics* **12**, 677 (2016), publisher: Nature Publishing Group.
- [10] X. Xu, W. Yao, D. Xiao, and T. F. Heinz, *Nature Physics* **10**, 343 (2014), publisher: Nature Publishing Group.
- [11] H. Zeng, J. Dai, W. Yao, D. Xiao, and X. Cui, *Nature Nanotechnology* **7**, 490 (2012), publisher: Nature Publishing Group.
- [12] J. Zipfel, M. Kulig, R. Perea-Causín, S. Brem, J. D. Ziegler, R. Rosati, T. Taniguchi, K. Watanabe, M. M. Glazov, E. Malic, and A. Chernikov, *Physical Review B* **101**, 115430 (2020), publisher: American Physical Society.
- [13] K. Wagner, E. Wietek, J. D. Ziegler, M. A. Semina, T. Taniguchi, K. Watanabe, J. Zipfel, M. M. Glazov, and A. Chernikov, *Physical Review Letters* **125**, 267401 (2020), publisher: American Physical Society.
- [14] K. Wagner, Z. A. Iakovlev, J. D. Ziegler, M. Cuccu, T. Taniguchi, K. Watanabe, M. M. Glazov, and A. Chernikov, *Nano Letters* **23**, 4708 (2023), publisher: American Chemical Society.
- [15] E. Wietek, M. Florian, J. Göser, T. Taniguchi, K. Watanabe, A. Högele, M. M. Glazov, A. Steinhoff, and A. Chernikov, *Physical Review Letters* **132**, 016202 (2024), publisher: American Physical Society.
- [16] R. Rosati, R. Perea-Causín, S. Brem, and E. Malic, *Nanoscale* **12**, 356 (2019), publisher: The Royal Society of Chemistry.
- [17] F. Tagarelli, E. Lopriore, D. Erkensten, R. Perea-Causín, S. Brem, J. Hagel, Z. Sun, G. Pasquale, K. Watanabe, T. Taniguchi, E. Malic, and A. Kis, *Nature Photonics* **17**, 615 (2023), publisher: Nature Publishing Group.
- [18] R. Rosati, R. Schmidt, S. Brem, R. Perea-Causín, I. Niehues, J. Kern, J. A. Preuß, R. Schneider, S. Michaelis de Vasconcellos, R. Bratschitsch, and E. Malic, *Nature Communications* **12**, 7221 (2021), publisher: Nature Publishing Group.
- [19] R. Rosati, K. Wagner, S. Brem, R. Perea-Causín, J. D. Ziegler, J. Zipfel, T. Taniguchi, K. Watanabe, A. Chernikov, and E. Malic, *Nanoscale* **13**, 19966 (2021), publisher: Royal Society of Chemistry.
- [20] F. Dirnberger, J. D. Ziegler, P. E. Faria Junior, R. Bushati, T. Taniguchi, K. Watanabe, J. Fabian, D. Bougeard, A. Chernikov, and V. M. Menon, *Science Advances* **7**, eabj3066 (2021), publisher: American Association for the Advancement of Science.
- [21] G. Moody, K. Tran, X. Lu, T. Autry, J. M. Fraser, R. P. Mirin, L. Yang, X. Li, and K. L. Silverman, *Physical Review Letters* **121**, 057403 (2018), publisher: American Physical Society.
- [22] G. Plechinger, P. Nagler, A. Arora, R. Schmidt, A. Chernikov, A. G. Del Águila, P. C. Christianen, R. Bratschitsch, C. Schüller, and T. Korn, *Nature Communications* **7**, 12715 (2016).
- [23] M. Ersfeld, F. Volmer, L. Rathmann, L. Kotewitz, M. Heithoff, M. Lohmann, B. Yang, K. Watanabe, T. Taniguchi, L. Bartels, J. Shi, C. Stampfer, and B. Beschoten, *Nano Letters* **20**, 3147 (2020).
- [24] C. Robert, D. Lagarde, F. Cadiz, G. Wang, B. Lassagne, T. Amand, A. Balocchi, P. Renucci, S. Tongay, B. Urbaszek, and X. Marie, *Physical Review B* **93**, 205423 (2016).
- [25] E. Malic, M. Selig, M. Feierabend, S. Brem, D. Christiansen, F. Wendlar, A. Knorr, and G. Berghäuser, *Physical Review Materials* **2**, 014002 (2018), publisher: American Physical Society.
- [26] M. Selig, G. Berghäuser, M. Richter, R. Bratschitsch, A. Knorr, and E. Malic, *2D Materials* **5**, 035017 (2018), publisher: IOP Publishing.
- [27] J. Lindlau, M. Selig, A. Neumann, L. Colombier, J. Förste, V. Funk, M. Förg, J. Kim, G. Berghäuser, T. Taniguchi, K. Watanabe, F. Wang, E. Malic, and A. Högele, *Nature Communications* **9**, 2586 (2018), publisher: Nature Publishing Group.
- [28] M. Selig, F. Katsch, R. Schmidt, S. Michaelis De Vasconcellos, R. Bratschitsch, E. Malic, and A. Knorr, *Physical Review Research* **1**, 022007 (2019).
- [29] M. Selig, F. Katsch, S. Brem, G. F. Mkrtchian, E. Malic, and A. Knorr, *Physical Review Research* **2**, 023322 (2020).
- [30] S. Beaulieu, S. Dong, V. Christiansson, P. Werner, T. Pincelli, J. D. Ziegler, T. Taniguchi, K. Watanabe, A. Chernikov, M. Wolf, L. Rettig, R. Ernstorfer, and M. Schüler, *Science Advances* **10**, eadk3897 (2024).
- [31] L. Linhart, M. Paur, V. Smejkal, J. Burgdörfer, T. Mueller, and F. Libisch, *Physical Review Letters* **123**, 146401 (2019), publisher: American Physical Society.
- [32] P. Hernández López, S. Heeg, C. Schattauer, S. Kovalchuk, A. Kumar, D. J. Bock, J. N. Kirchhof, B. Höfer, K. Greben, D. Yagodkin, L. Linhart, F. Libisch, and K. I. Bolotin, *Nature Communications* **13**, 7691 (2022), publisher: Nature Publishing Group.
- [33] K. Zollner, P. E. F. Junior, and J. Fabian, *Physical Review B* **100**, 195126 (2019), publisher: American Physical Society.
- [34] A. M. Kumar, D. Yagodkin, R. Rosati, D. J. Bock, C. Schattauer, S. Tobisch, J. Hagel, B. Höfer, J. N. Kirchhof, P. Hernández López, K. Burfeindt, S. Heeg, C. Gahl, F. Libisch, E. Malic, and K. I. Bolotin, *Nature Communications* **15**, 7546 (2024), publisher: Nature Publishing Group.

- [35] Z. Khatibi, M. Feierabend, M. Selig, S. Brem, C. Linderälv, P. Erhart, and E. Malic, *2D Materials* **6**, 015015 (2018), publisher: IOP Publishing.
- [36] X.-X. Zhang, T. Cao, Z. Lu, Y.-C. Lin, F. Zhang, Y. Wang, Z. Li, J. C. Hone, J. A. Robinson, D. Smirnov, S. G. Louie, and T. F. Heinz, *Nature Nanotechnology* **12**, 883 (2017), publisher: Nature Publishing Group.
- [37] Y. Zhou, G. Scuri, D. S. Wild, A. A. High, A. Dibos, L. A. Jauregui, C. Shu, K. De Greve, K. Pistunova, A. Y. Joe, T. Taniguchi, K. Watanabe, P. Kim, M. D. Lukin, and H. Park, *Nature Nanotechnology* **12**, 856 (2017), publisher: Nature Publishing Group.
- [38] Y. Tang, K. F. Mak, and J. Shan, *Nature Communications* **10**, 4047 (2019), publisher: Nature Publishing Group.
- [39] Z. Li, T. Wang, C. Jin, Z. Lu, Z. Lian, Y. Meng, M. Blei, M. Gao, T. Taniguchi, K. Watanabe, T. Ren, T. Cao, S. Tongay, D. Smirnov, L. Zhang, and S.-F. Shi, *ACS Nano* **13**, 14107 (2019), publisher: American Chemical Society.
- [40] T. Deilmann and K. S. Thygesen, *2D Materials* **6**, 035003 (2019), publisher: IOP Publishing.
- [41] R. Rosati, K. Wagner, S. Brem, R. Perea-Causín, E. Witek, J. Zipfel, J. D. Ziegler, M. Selig, T. Taniguchi, K. Watanabe, A. Knorr, A. Chernikov, and E. Malic, *ACS Photonics* **7**, 2756 (2020), publisher: American Chemical Society.
- [42] S. Brem, A. Ekman, D. Christiansen, F. Katsch, M. Selig, C. Robert, X. Marie, B. Urbaszek, A. Knorr, and E. Malic, *Nano Letters* **20**, 2849 (2020), publisher: American Chemical Society.
- [43] I. Niehues, R. Schmidt, M. Drüppel, P. Marauhn, D. Christiansen, M. Selig, G. Berghäuser, D. Wigger, R. Schneider, L. Braasch, R. Koch, A. Castellanos-Gomez, T. Kuhn, A. Knorr, E. Malic, M. Rohlfing, S. Michaelis de Vasconcellos, and R. Bratschitsch, *Nano Letters* **18**, 1751 (2018).
- [44] B. Aslan, M. Deng, and T. F. Heinz, *Physical Review B* **98**, 115308 (2018), publisher: American Physical Society.
- [45] M. G. Harats, J. N. Kirchhof, M. Qiao, K. Greben, and K. I. Bolotin, *Nature Photonics* **14**, 324 (2020), publisher: Nature Publishing Group.
- [46] S. Kovalchuk, M. G. Harats, G. López-Polín, J. N. Kirchhof, K. Höflich, and K. I. Bolotin, *2D Materials* **7**, 035024 (2020).
- [47] M. Feierabend, A. Morlet, G. Berghäuser, and E. Malic, *Physical Review B* **96**, 045425 (2017), publisher: American Physical Society.
- [48] P. Rivera, M. He, B. Kim, S. Liu, C. Rubio-Verdú, H. Moon, L. Mennel, D. A. Rhodes, H. Yu, T. Taniguchi, K. Watanabe, J. Yan, D. G. Mandrus, H. Dery, A. Pasupathy, D. Englund, J. Hone, W. Yao, and X. Xu, *Nature Communications* **12**, 871 (2021), publisher: Nature Publishing Group.
- [49] M. He, P. Rivera, D. Van Tuan, N. P. Wilson, M. Yang, T. Taniguchi, K. Watanabe, J. Yan, D. G. Mandrus, H. Yu, H. Dery, W. Yao, and X. Xu, *Nature Communications* **11**, 618 (2020), publisher: Nature Publishing Group.
- [50] E. Liu, J. Van Baren, T. Taniguchi, K. Watanabe, Y.-C. Chang, and C. H. Lui, *Physical Review Research* **1**, 032007 (2019).
- [51] M. Selig, G. Berghäuser, A. Raja, P. Nagler, C. Schüller, T. F. Heinz, T. Korn, A. Chernikov, E. Malic, and A. Knorr, *Nature Communications* **7**, 13279 (2016), publisher: Nature Publishing Group.
- [52] G. Wang, C. Robert, M. Glazov, F. Cadiz, E. Courtade, T. Amand, D. Lagarde, T. Taniguchi, K. Watanabe, B. Urbaszek, and X. Marie, *Physical Review Letters* **119**, 047401 (2017).
- [53] Z. Li, T. Wang, Z. Lu, M. Khatoniar, Z. Lian, Y. Meng, M. Blei, T. Taniguchi, K. Watanabe, S. A. McGill, S. Tongay, V. M. Menon, D. Smirnov, and S.-F. Shi, *Nano Letters* **19**, 6886 (2019), publisher: American Chemical Society.
- [54] C. Robert, S. Park, F. Cadiz, L. Lombez, L. Ren, H. Tornatzky, A. Rowe, D. Paget, F. Sirotti, M. Yang, D. Van Tuan, T. Taniguchi, B. Urbaszek, K. Watanabe, T. Amand, H. Dery, and X. Marie, *Nature Communications* **12**, 5455 (2021), publisher: Nature Publishing Group.
- [55] H. Yu, G.-B. Liu, P. Gong, X. Xu, and W. Yao, *Nature Communications* **5**, 3876 (2014), publisher: Nature Publishing Group.
- [56] Y.-C. Wu, T. Taniguchi, K. Watanabe, and J. Yan, *Physical Review B* **104**, L121408 (2021).
- [57] M. Z. Maialle, E. A. De Andrada E Silva, and L. J. Sham, *Physical Review B* **47**, 15776 (1993).
- [58] Z. An, P. Soubelet, Y. Zhumagulov, M. Zopf, A. Delhomme, C. Qian, P. E. Faria Junior, J. Fabian, X. Cao, J. Yang, A. V. Stier, F. Ding, and J. J. Finley, *Physical Review B* **108**, L041404 (2023), publisher: American Physical Society.
- [59] R. Rosati, S. Brem, R. Perea-Causín, R. Schmidt, I. Niehues, S. M. d. Vasconcellos, R. Bratschitsch, and E. Malic, *2D Materials* **8**, 015030 (2020), publisher: IOP Publishing.
- [60] F. Volmer, S. Pissinger, M. Ersfeld, S. Kuhlen, C. Stampfer, and B. Beschoten, *Physical Review B* **95**, 235408 (2017), publisher: American Physical Society.
- [61] L. Yang, N. A. Sinitsyn, W. Chen, J. Yuan, J. Zhang, J. Lou, and S. A. Crooker, *Nature Physics* **11**, 830 (2015), publisher: Nature Publishing Group.
- [62] P. Dey, L. Yang, C. Robert, G. Wang, B. Urbaszek, X. Marie, and S. Crooker, *Physical Review Letters* **119**, 137401 (2017), publisher: American Physical Society.
- [63] J. Li, M. Goryca, K. Yumigeta, H. Li, S. Tongay, and S. A. Crooker, *Physical Review Materials* **5**, 044001 (2021), publisher: American Physical Society.
- [64] M. M. Glazov, F. Dirnberger, V. M. Menon, T. Taniguchi, K. Watanabe, D. Bougeard, J. D. Ziegler, and A. Chernikov, *Physical Review B* **106**, 125303 (2022), publisher: American Physical Society.
- [65] Z. A. Iakovlev and M. M. Glazov, *2D Materials* **10**, 035034 (2023), publisher: IOP Publishing.
- [66] D. Yagodkin, K. Burfeindt, Z. A. Iakovlev, A. M. Kumar, A. Dewambrechies, O. Yücel, B. Höfer, C. Gahl, M. M. Glazov, and K. I. Bolotin, "Excitons under large pseudo-magnetic fields," (2024), arXiv:2412.16596 [cond-mat].
- [67] J. J. P. Thompson, S. Brem, M. Verjans, R. Schmidt, S. M. d. Vasconcellos, R. Bratschitsch, and E. Malic, *2D Materials* **9**, 025008 (2022), publisher: IOP Publishing.
- [68] N. S. Rytova, *Proc. MSU, Phys., Astron.* **3**, 30 (1967).
- [69] L. Keldysh, *JETP Letters* **29**, 658 (1979).
- [70] A. Kormányos, G. Burkard, M. Gmitra, J. Fabian, V. Zólyomi, N. D. Drummond, and V. Fal'ko, *2D Materials* **2**, 022001 (2015), publisher: IOP Publishing.